

WATER, METHANE DEPLETION, AND HIGH-ALTITUDE CONDENSATES IN THE ATMOSPHERE OF THE WARM SUPER-NEPTUNE WASP-107b

LAURA KREIDBERG^{1,2}

MICHAEL R. LINE³

DANIEL THORNGREN⁴

CAROLINE V. MORLEY^{2,*}

KEVIN B. STEVENSON⁵

¹*Harvard Society of Fellows 78 Mt. Auburn St.
Cambridge, MA 02138, USA*

²*Harvard-Smithsonian Center for Astrophysics 60 Garden St.
Cambridge, MA 02138*

³*Arizona State University*

⁴*University of California Santa Cruz*

⁵*Space Telescope Science Institute*

Submitted to ApJL

ABSTRACT

The super-Neptune exoplanet WASP-107b is an exciting target for atmosphere characterization. It has an unusually large atmospheric scale height and a small, bright host star, raising the possibility of precise constraints on its current nature and formation history. We report the first atmospheric study of WASP-107b, a Hubble Space Telescope measurement of its near-infrared transmission spectrum. We determined the planet’s composition with two techniques: atmospheric retrieval based on the transmission spectrum and interior structure modeling based on the observed mass and radius. The interior structure models set a 3σ upper limit on the atmospheric metallicity of $30\times$ solar. The transmission spectrum shows strong evidence for water absorption (6.5σ confidence), and we infer a water abundance consistent with expectations for a solar abundance pattern. On the other hand, methane is depleted relative to expectations (at 3σ confidence), suggesting a low carbon-to-oxygen ratio or high internal heat flux. The water features are smaller than predicted for a cloudless atmosphere, crossing less than one scale height. A thick condensate layer at high altitudes (0.1 - 3 mbar) is needed to match the observations; however, we find that it is challenging for physically motivated cloud and haze models to produce opaque condensates at these pressures. Taken together, these findings serve as an illustration of the diversity and complexity of exoplanet atmospheres. The community can look forward to more such results with the high precision and wide spectral coverage afforded by future observing facilities.

Keywords: planets and satellites: individual (WASP-107b), planets and satellites: atmospheres

Corresponding author: Laura Kreidberg
laura.kreidberg@cfa.harvard.edu

* Sagan Fellow

1. INTRODUCTION

The composition of a planet’s atmosphere depends on where and how the planet formed. By measuring the inventory of atmospheric elemental abundances, we can shed light on important aspects of the formation process such as location within the disk and the relative accretion rates of gas versus solids (Öberg et al. 2011; Fortney et al. 2013; Madhusudhan et al. 2014; Mordasini et al. 2016; Espinoza et al. 2017).

The warm Neptune WASP-107b is an intriguing target for atmosphere characterization for several reasons. It has an intermediate size between ice giants and gas giants, with a mass similar to Neptune’s and a radius close to Jupiter’s ($0.12 M_{\text{Jup}}$, $0.94 R_{\text{Jup}}$; Anderson et al. 2017). Studying the atmospheres of planets in this transition region will provide additional clues in the much-debated mystery of what stunts the growth of Neptune-size planets (e.g. Pollack et al. 1996; Dawson et al. 2016; Frelikh & Murray-Clay 2017).

WASP-107b also has a relatively low equilibrium temperature compared to most other exoplanets that are amenable to atmosphere characterization (780 K, assuming zero albedo). This results in a distinct atmospheric chemistry from other well-studied systems: at low temperatures, the dominant molecular reservoir for carbon transitions from carbon monoxide to methane (Moses et al. 2013). Spectral features from both water and methane are accessible with current observing facilities, enabling a spectroscopic estimate of the carbon-to-oxygen ratio (C/O). Previous measurements of C/O have been challenging because they rely on broadband photometry or narrow wavelength coverage (e.g. Madhusudhan et al. 2011; Line et al. 2014; Benneke 2015; Kreidberg et al. 2015).

In addition, WASP-107b is one of the best targets discovered to date for atmosphere characterization. Thanks to its large atmospheric scale height and small, bright host star, the expected signal-to-noise for the transmission spectrum is comparable to the best studied benchmarks in the field (e.g. HD 209458b). In this paper we report the first atmosphere characterization of WASP-107b: a near-infrared transmission spectrum measured with the *Hubble Space Telescope* (HST; Program GO 14915, PI L. Kreidberg).

2. OBSERVATIONS AND DATA REDUCTION

We observed a single transit of WASP-107b with HST’s Wide Field Camera 3 (WFC3) instrument on UT 5-6 June 2017. The transit observation consisted of five HST orbits. At the beginning of each 96-minute orbit, we took an image of the target with the F130N filter (exposure time = 4.2 s). This direct image is used for wave-

length calibration. For the remainder of the target visibility period, we obtained time series spectra with the G141 grism, which provides low-resolution spectroscopy over the wavelength range $1.1 - 1.7 \mu\text{m}$. We used the NSAMP=6, SPARS.25 readout mode (exposure time = 112 s) to optimize the efficiency of the observations, as determined by the PandExo-HST planning tool (Batalha et al. 2017). As is standard for WFC3 observations of bright targets, we used the spatial scanning observing mode, which slews the telescope in the spatial direction over the course of an exposure. The scan rate was 0.12 arcseconds/sec.

We reduced the data with the custom pipeline described in Kreidberg et al. (2014a), which we summarize briefly here. For each exposure, we extracted the spectrum from each up-the-ramp sample (or “stripe”) separately using the optimal extraction algorithm of Horne (1986). We estimated the background from the median count level of pixels uncontaminated by the target spectrum (rows 5–250, columns 5–515). The stripe spectra were then summed to create the final spectrum. For each stripe, the extraction box was 80 pixels high and centered on the stripe’s midpoint in the spatial direction. We corrected the spectra for the changing dispersion solution over this aperture and small drifts over time (< 0.1 pixel).

3. LIGHT CURVE ANALYSIS

The data analysis had two parts: the band-integrated “white” light curve fit and the spectroscopic light curve fits.

3.1. White Light Curve

To create the raw white light curve, we summed each spectrum over the 181 pixels in the spectral trace. The white light curve has systematic trends that are typical for WFC3 observations (Zhou et al. 2017): the flux increases asymptotically over each orbit (the “ramp” effect) and there is a visit-long linear trend. The largest ramp occurs in the initial orbit (orbit zero), so we only fit data from orbits one through four in our analysis, following common practice. We fit the light curve with the analytic model of the form $F_{\text{white}}(t) = S_{\text{white}}(t) \times T_{\text{white}}(t)$, where S_{white} is a systematics model and T_{white} is a transit model. We used the same systematics model as Kreidberg et al. (2015). We modelled the transit with the batman package (Kreidberg 2015). The model parameters are the orbital period p , time of inferior conjunction t_0 , transit depth r_p/r_s , ratio of semi-major axis to stellar radius a/r_s , orbital inclination i , and the quadratic stellar limb darkening parameters u_1 and u_2 .

3.1.1. Star Spot Crossing

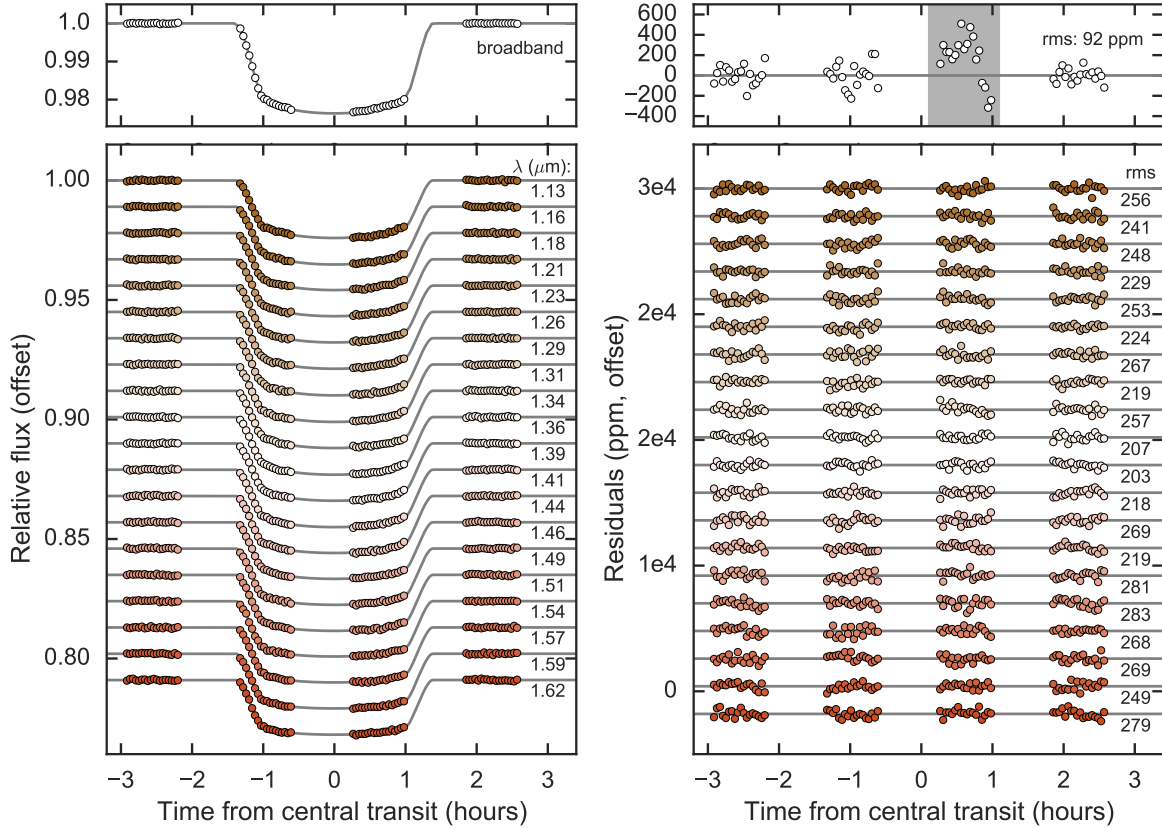


Figure 1. Left: Broadband and spectrophotometric transit light curves for WASP-107b compared to best fit models. Right: residuals from the best fit. Annotations indicate the central wavelength and root-mean-square (rms) residuals. A star-spot crossing feature is shaded in gray in the upper right; our systematic error correction removes this feature from the spectroscopic light curves.

In our initial analysis, we noticed a bump in the light curve during orbit three that was not fit well with our model. We attribute this feature to a star spot crossing event, as WASP-107 is an active star and spot crossings have been observed before (Dai & Winn 2017; Moćnik et al. 2017). In our subsequent analysis, we gave the data in orbit three no weight in the fit. The amplitude of the spot crossing feature is 300 ppm, as illustrated in Figure 1.

3.1.2. Final Fit

In our final fit, we fixed the transit parameters a/r_s , i , p on the precise estimates from the Kepler light curve (Dai & Winn 2017). We also fixed quadratic limb darkening parameters u_1 and u_2 on predictions from a PHOENIX model for a star with effective temperature 4300 K, calculated with the `limb-darkening` package from Espinoza & Jordán (2015). We checked that the values we fixed were consistent with our estimates when we allowed them to vary freely. We also checked that the

uncertainty in the stellar parameters does not affect the PHOENIX model predictions at the level of precision of our data: we varied the stellar effective temperature by ± 100 K from the published value and found that the transmission spectrum was not significantly changed. The remaining free parameters in the fit were t_0 , r_p/r_s , and the systematics parameters for the visit-long and orbit-long trends.

For the best fit white light curve, the root-mean-square (rms) residuals were 93 ppm (excluding the star spot crossing), which is somewhat larger than the expected shot noise of 50 ppm. We attribute the excess noise to loss of flux off the edge of the detector, which can occur if there is variation in the position or length of the spatial scan. There is no evidence for correlated noise in the residuals, so to account for the excess noise we simply increased the per-point uncertainties by a factor of 1.7 to achieve a χ^2_ν value of unity. We then used the Markov chain Monte

Carlo (MCMC) algorithm to estimate parameter uncertainties (Foreman-Mackey et al. 2013). The chain had 50 walkers which each ran for 10^4 steps with the first 10% discarded as burn-in. We tested for convergence by dividing the chain in two halves and confirming that they gave consistent results. The transit time was $t_0 = 2457910.45407 \pm 6e-5$ BJD_{TDB} and the planet/star radius was $r_p/r_s = 0.14399 \pm 0.00017$.

3.2. Spectroscopic Light Curve Fits

We binned the spectrum into 20 spectrophotometric channels from 1.12 to 1.63 μm , shown in Figure 1. We fit the light curves with the `divide-white` technique, which assumes that the light curve systematics have the same morphology at all wavelengths (Stevenson et al. 2014; Kreidberg et al. 2014a). For this method, the transit model $T_\lambda(t)$ is multiplied by the systematics vector from the white light curve fit ($F_{\text{white}}/T_{\text{white}}$), and rescaled by a factor $C_\lambda + V_\lambda t$. One advantage of this approach is that it removes the star spot crossing feature, enabling us to use orbit three with no additional correction. The amplitude of the feature has no detectable wavelength dependence at the level of precision of our data. As for the white light curve, we fixed some of the transit parameters on the best fit values from Dai & Winn (2017). We did not put priors on the transit parameters because varying them simply shifts the spectrum up or down by a constant value. Since the planet’s 10-bar radius is a free parameter in our analysis of the spectrum, the absolute transit depth does not affect the retrieved atmospheric properties. In addition to fixing the transit parameters, we also fixed the limb darkening on the PHOENIX model predictions (coefficients listed in Table 1).

The final spectroscopic light curve fits had just three free parameters per channel: C_λ , V_λ , and r_p/r_s .

The best fit light curves have a median χ_ν^2 value of 1.16. We conservatively rescaled the photometric uncertainties for all spectroscopic channels such that the χ_ν^2 values are unity. We performed an MCMC fit to the light curves with `emcee`. For each light curve we ran a fit with 50 walkers and 1000 steps per walker, and tested for convergence as we did for the white light curve. The median transit depths and 1σ uncertainties are given in Table 1.

We explored several alternative choices for the spectroscopic light curve fits, but found that none of them made a significant difference in the transmission spectrum. In one test, we fit the spectroscopic light curves with the same analytic model we used for the white light curve. We also tested a white light curve systematics vector S_{white} from a fit that included the star-spot

Table 1. WASP-107b transmission spectrum and limb darkening coefficients

Wavelength (μm)	Transit depth	Uncertainty	u_1	u_2
1.121 – 1.145	0.020641	5.9e-05	0.38	0.13
1.145 – 1.171	0.020733	5.5e-05	0.37	0.14
1.171 – 1.196	0.020505	5.6e-05	0.36	0.14
1.196 – 1.222	0.020498	5.4e-05	0.36	0.15
1.222 – 1.248	0.020455	5.9e-05	0.36	0.15
1.248 – 1.272	0.020492	5.0e-05	0.35	0.16
1.272 – 1.298	0.020620	6.2e-05	0.34	0.17
1.298 – 1.323	0.020739	5.0e-05	0.34	0.17
1.323 – 1.349	0.020660	5.7e-05	0.33	0.18
1.349 – 1.374	0.020858	4.8e-05	0.32	0.19
1.374 – 1.401	0.020794	4.8e-05	0.31	0.20
1.401 – 1.425	0.020888	5.2e-05	0.30	0.21
1.425 – 1.452	0.020821	6.2e-05	0.29	0.21
1.452 – 1.476	0.020691	5.1e-05	0.28	0.22
1.476 – 1.502	0.020682	6.9e-05	0.26	0.23
1.502 – 1.528	0.020679	6.7e-05	0.25	0.23
1.528 – 1.552	0.020509	6.0e-05	0.23	0.25
1.552 – 1.579	0.020480	6.4e-05	0.22	0.24
1.579 – 1.603	0.020500	5.6e-05	0.20	0.24
1.603 – 1.629	0.020514	6.5e-05	0.19	0.25

crossing orbit. The results from these tests are nearly identical to our nominal transmission spectrum (differing by $< 0.5\sigma$ on average), except with a small constant offset due to the uncorrected star-spot crossing feature. This offset does not affect our final analysis because it is marginalized in the atmospheric retrieval with the 10-bar radius parameter (see § 4.2).

We also fit for a linear limb darkening parameter rather than fixing the limb darkening on the PHOENIX model values. We found that the fitted limb darkening coefficients are consistent with the model predictions, so we opted to fix the coefficients in our final analysis because it improves the precision on the transit depths by about 10%. We also performed an independent data reduction and fit using K. Stevenson’s pipeline and found consistent results (well within 1σ).

4. COMPOSITION OF THE ATMOSPHERE

In this section we discuss constraints on the composition of WASP-107b’s atmosphere based on inte-

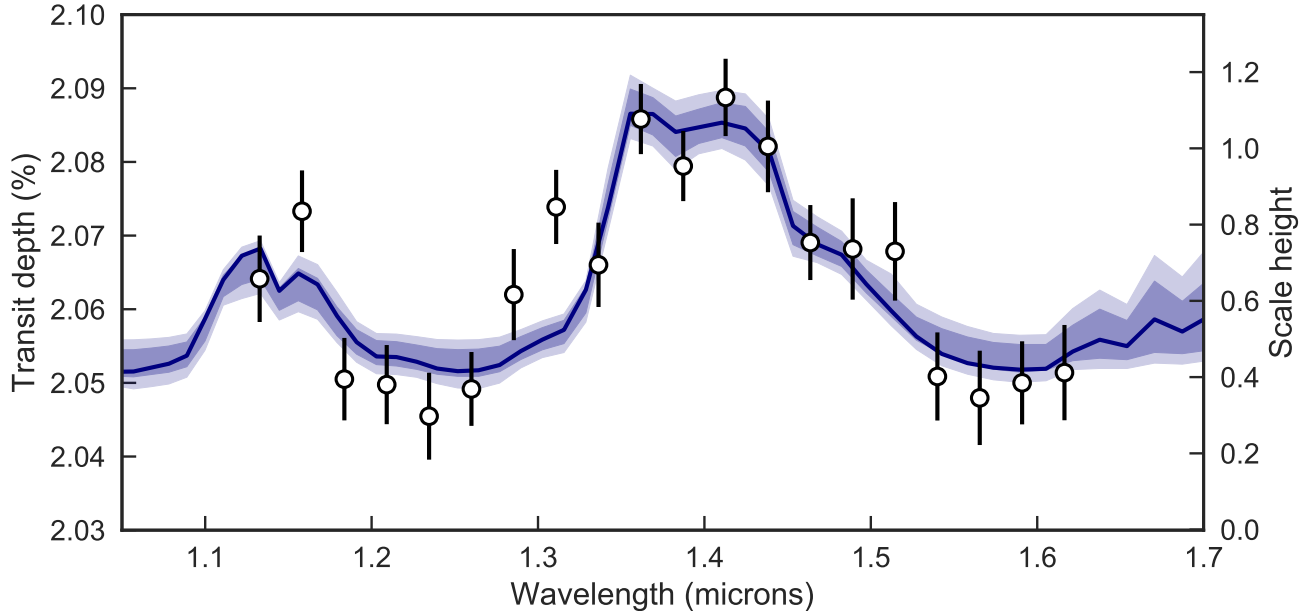


Figure 2. The transmission spectrum of WASP-107b (points with 1σ error bars) compared to retrieved models (blue line with shaded 1 and 2σ confidence intervals). The features at 1.15 and $1.4\ \mu\text{m}$ are due to water absorption. The right-hand axis indicates the normalized atmospheric scale height assuming solar composition. The water feature crosses less than one scale height, indicating that condensates are present at high altitude.

rior structure modeling and atmospheric retrieval of the measured transmission spectrum.

4.1. Atmospheric Metallicity from Interior Structure Modeling

Given WASP-107b’s unusually low density, we quantitatively explored the range of atmospheric metallicities that are consistent with the observed mass and radius using the structure evolution modeling of [Thorngrén et al. \(2016\)](#). These models assume a thermally inert heavy-element core with a convective envelope of additively mixed H/He ([Saumon et al. 1995](#)) and heavy-element impurities. The heavy elements were a 50-50 rock-ice mix. We evolved the planets in time using the atmospheric models of [Fortney et al. \(2007\)](#). The results are sensitive to assumptions about the stellar age, which is uncertain (either 0.6 ± 0.2 to 8.3 ± 4.3 Gyr depending on model assumptions; [Močnik et al. 2017](#)). We therefore ran two models, with uniform age priors of either $0.2 - 1.0$ or $1.0 - 13.8$ Gyr. We used the published mass and radius estimates ($0.12 \pm 0.01 M_J$, 0.94 ± 0.02 ; [Anderson et al. 2017](#)).

Based on these assumptions, we fit for envelope metallicity and core mass using an MCMC with uniform priors on both parameters. The MCMC burned in for 10^3 steps and then collected 4×10^6 samples. The envelope metal mass fractions were converted to metallicities assuming

the mean molecular weight of the metals was 18 (the value for water), using the approach of [Fortney et al. \(2013\)](#). Figure 3 shows the results. We find a 3σ upper limit on the metallicity of $30\times$ solar for the young stellar age range. Higher metallicity envelopes are not allowed because they decrease the planet’s radius below the observed value. For the older age, the upper limit is even lower ($20\times$ solar), because planets cool and contract as they age ([Fortney et al. 2008](#)). The largest sources of uncertainty in the metallicity estimate are the unknown core mass and stellar age, which are dominant over modeling uncertainties due to the equation of state and distribution of heavy elements in the envelope ([Thorngrén et al. 2016](#)). By marginalizing over the unknown physical parameters, we obtain a conservative upper limit on the envelope metallicity. Realistically, the planet probably formed with a core. Assuming a $5 M_\oplus$ core, the upper limit on metallicity is 20 (10) M_\oplus for the young (old) age.

4.2. Retrieval

We also inferred the composition of the atmosphere directly from the transmission spectrum using the CHIMERA chemically-consistent retrieval ([Line et al. 2013](#)). Briefly, CHIMERA solves the transmission geometry problem using the equations in [Brown \(2001\)](#); [Tinetti et al. \(2012\)](#). We parameterized atmospheric

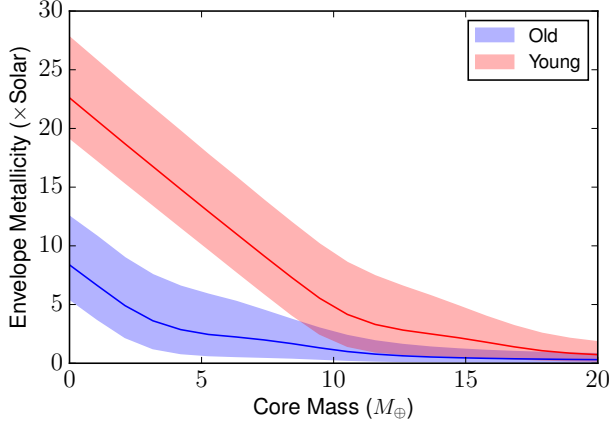


Figure 3. Estimated envelope metallicity for a given core mass based on interior structure modeling. The red shading corresponds to the 1σ confidence interval for a young planet (0.2 – 1 Gyr); the blue is for an older age (1 – 14 Gyr).

composition with metallicity and carbon-to-oxygen ratio under the assumption of thermochemical equilibrium using the NASA CEA routine (Gordon & McBride 1994) to compute the molecular abundances for H_2 , He, H_2O , CH_4 , CO, CO_2 , NH_3 , H_2S , Na, K, HCN, C_2H_2 , TiO, VO, and FeH. We updated the transmission model to use correlated-K opacities (Lacis & Oinas 1991; Mollière et al. 2015; Amundsen et al. 2016) from the pre-tabulated line-by-line cross section database described in Freedman et al. (2014). The transmission forward model is coupled with the PyMultiNest tool (Buchner 2016) to solve the parameter estimation and model selection problems.

Our nominal model included a temperature-pressure profile (parameterized via the Guillot 2010 relations), the atmospheric metallicity, the C/O, a gray cloud-top pressure, and the planet’s 10-bar radius. We fixed the T-P profile morphology but scaled the irradiation temperature to allow for the unknown albedo and heat transport efficiency. We put a uniform prior on the atmospheric metallicity of $0.01 - 30\times$ solar based on the upper limit from § 4.1.

The nominal retrieval results are shown in Figure 4. The best fit model provides a good fit to the data ($\chi^2_\nu = 1.2$). The metallicity distribution spans the full range allowed by our priors, with preference for larger values. The cloud top pressure is estimated to be $0.01 - 3$ mbar at 1σ confidence. The retrieved irradiation temperature is $525 - 820$ K (1σ confidence). We find that the C/O value is less than solar (0.54) at 2.7σ confidence. We tested the detection significance for water by removing water opacity from the nominal model. The Bayesian evidence favors the inclusion of water at 6.5σ confidence.

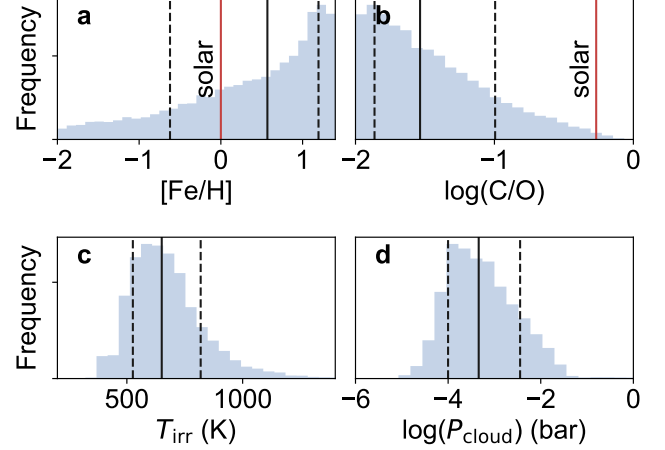


Figure 4. Retrieved distributions for (a) metallicity, (b) carbon-to-oxygen ratio, (c) irradiation temperature, and (d) cloud-top pressure in bars. Black vertical lines show the median and $\pm 1\sigma$ confidence interval (solid and dashed, respectively). Solar metallicity and C/O values are indicated with red vertical lines.

We explored a few retrieval scenarios with additional complexity, including the addition of cloud patchiness (Line et al. 2016), a quench pressure for nitrogen and carbon species (e.g. Morley et al. 2017), and a power law haze opacity. We also varied the assumed planet mass by 3σ . These models did not significantly improve the fit quality, and the main retrieval results were unchanged. We also explored cases without the $30\times$ solar metallicity prior upper limit. Without this prior, metallicities up to $100\times$ were permitted, but other parameters were not significantly changed.

4.2.1. Methane Abundance

We ran two additional retrievals to explore whether methane depletion is the underlying cause of the inferred low C/O. Even though water is the dominant absorber in the WFC3 bandpass, there is enough methane opacity to change the shape of the spectral features at a detectable level for high precision data. In one test, we assumed chemical equilibrium but excluded methane opacity. This set-up resulted in a much broader distribution of C/O values ($0.02 - 1.6$ at 1σ).

We also performed a “free” retrieval that varied the abundances of CH_4 , H_2O and NH_3 with no assumption of chemical equilibrium. The 3σ upper limit on methane abundance is 1.2×10^{-3} , ruling out the predicted equilibrium methane content at photospheric temperature and pressure (700 Kelvin, 10 mbar), for a composition with solar C/O and $3\times$ solar metallicity. We chose $3\times$ solar as a benchmark for comparison because this

is the median metallicity from the chemical equilibrium retrieval. Based on these tests, we conclude that the atmosphere of WASP-107b is depleted in methane relative to expectations for a solar abundance pattern. By contrast, the water abundance ($6 \times 10^{-6} - 2 \times 10^{-3}$) is consistent with predictions for solar composition.

4.3. Condensate Properties

In addition to the atmospheric retrieval, we also performed forward modeling of physically motivated, self-consistent clouds and hazes using the methods described in Fortney et al. (2008); Morley et al. (2015). We model clouds that form in cool atmospheres (Na_2S , KCl , ZnS ; see Morley et al. 2012), for a range of metallicities from $1 - 50\times$ solar. We vary the cloud sedimentation efficiency from 3 to 0.1 (normal to highly lofted, small particulate clouds). None of the models produce sufficiently low amplitude spectral features to match the observed spectrum. This result suggests that if clouds are muting WASP-107b’s transmission spectrum, the mechanism for cloud particle formation and vertical lofting is very efficient and not captured by the modeling used here. Further studies of cloud formation in very low gravity environments are required.

We also model an *ad hoc* photochemical “soot” layer near the top of the atmosphere. We predict the abundance of hydrocarbon haze precursors from previously published photochemical models for GJ 436b (Line et al. 2011; Morley et al. 2017). With the most efficient haze production (100% of precursors form haze) and particle sizes around 0.03 – 0.1 microns, the amplitude of the model water feature matches that of the observations.

These photochemical hazes are assumed to form from hydrocarbons generated by methane photolysis; however, we found in the previous section that methane is depleted. Furthermore, even if the precursors were present, it is unclear whether the 100% haze production efficiency is realistic. However, organic hydrocarbons are not the only possible photolytic haze in cool H_2 -rich atmospheres, as sulfur chemistry may create additional haze material (Zahnle et al. 2009; Gao et al. 2017). Further modeling and laboratory work of the hazes that form in these conditions is needed for a satisfactory explanation of the data.

5. DISCUSSION AND CONCLUSIONS

We analyzed the atmospheric composition of WASP-107b based on retrieval of its near-infrared transmission spectrum and interior structure models of the planet’s mass and radius. Key results from this analysis include:

- *The upper limit on atmospheric metallicity from interior structure modeling is $30\times$ solar.* This

limit is at the edge of consistency with the Solar System metal enrichment trend, which predicts a metallicity of $30\times$ solar for WASP-107b (Kreidberg et al. 2014b). Compared to results for other exoplanets of similar mass such as GJ 436b, which has a high metallicity ($> 100\times$ solar) and HAT-P-26b, which is metal-poor compared to the Solar System trend, WASP-107b adds to the evidence that exoplanets exhibit a greater diversity of compositions than is present in the Solar System (Morley et al. 2017; Wakeford et al. 2017).

- *The methane abundance is depleted relative to expectations for a solar abundance pattern, whereas water is consistent with solar composition.* This may be due to an intrinsically low carbon-to-oxygen ratio, which could arise from accretion of water-rich planetesimals (Mordasini et al. 2016; Espinoza et al. 2017). Another possibility is that the planet has a hot interior effective temperature (~ 500 K), and abundances are quenched at pressure levels where CO is stable (as observed in some directly imaged planets; Skemer et al. 2014; Zahnle & Marley 2014). Such a high internal temperature could be due to latent heat of formation if the planet is very young, and/or tidal heating (Fortney et al. 2008; Morley et al. 2017). Further observations of the transmission spectrum over a broader wavelength range will refine the C/O estimate and help differentiate between these two scenarios.
- *Optically thick condensates are present at high altitudes (0.1 – 3 mbar).* The amplitude of the water absorption feature in the transmission spectrum is less than a third that expected for a clear atmosphere. Existing models of physically-motivated cloud and haze formation do not satisfactorily reproduce the data. All the cloud models we consider produce condensation too deep in the atmosphere. Efficient hydrocarbon haze production at high altitudes can match the data, but these require the presence of methane to serve as a haze precursor. Other precursors such as H_2S are a possibility and would be worth exploring in future analyses. Put in context with other systems, the muted water feature for WASP-107b agrees well with the trend in feature amplitude with temperature noted in Crossfield & Kreidberg (2017), indicating that condensates may be common in the atmospheres of the coolest planets.

These results are a first look at the atmosphere of WASP-107b. It joins the ranks of two other relatively

cool, relatively low mass exoplanets with detected water features (HAT-P-11b and HAT-P-26b; [Fraine et al. 2014](#); [Wakeford et al. 2017](#)). WASP-107b is already the target of additional observing programs at other wavelengths, including the WFC3/G102 grism and Spitzer 3.6 and 4.5 μm channels in transit and eclipse (*HST* Program GO 14916, PI J. Spake, *Spitzer* Program 13052, PI M. Werner; *Spitzer* Program 13167, PI L. Kreidberg). In addition, WASP-107b is included in the *JWST* Guaranteed Time Observations for the NIRISS, NIRCAM, and NIRSpec instruments¹. This spate of observing pro-

grams is sure to add to the already rich and complex picture of WASP-107b’s atmosphere presented here.

New references [McCullough et al. \(2014\)](#); [Zellem et al. \(2017\)](#); [Griffith \(2014\)](#); [Heng & Kitzmann \(2017\)](#); [Rackham et al. \(2018\)](#); [de Wit & Seager \(2013\)](#).

We thank Fei Dai, Jessica Spake, Ian Crossfield, Hannah Diamond-Lowe, and Jonathan Fortney for productive conversations. L.K. acknowledges support from the Harvard Society of Fellows and the Harvard Astronomy Department Institute for Theory and Computation. C.V.M. acknowledges support from NASA through the Sagan Fellowship Program.

REFERENCES

- Amundsen, D. S., Mayne, N. J., Baraffe, I., et al. 2016, *A&A*, 595, A36
- Anderson, D. R., Collier Cameron, A., Delrez, L., et al. 2017, ArXiv e-prints, arXiv:1701.03776
- Batalha, N. E., Mandell, A., Pontoppidan, K., et al. 2017, *PASP*, 129, 064501
- Benneke, B. 2015, ArXiv e-prints, arXiv:1504.07655
- Brown, T. M. 2001, *ApJ*, 553, 1006
- Buchner, J. 2016, PyMultiNest: Python interface for MultiNest, Astrophysics Source Code Library, , , ascl:1606.005
- Crossfield, I. J. M., & Kreidberg, L. 2017, ArXiv e-prints, arXiv:1708.00016
- Dai, F., & Winn, J. N. 2017, *AJ*, 153, 205
- Dawson, R. I., Lee, E. J., & Chiang, E. 2016, *ApJ*, 822, 54
- de Wit, J., & Seager, S. 2013, *Science*, 342, 1473
- Espinoza, N., Fortney, J. J., Miguel, Y., Thorngren, D., & Murray-Clay, R. 2017, *ApJL*, 838, L9
- Espinoza, N., & Jordán, A. 2015, *MNRAS*, 450, 1879
- Foreman-Mackey, D., Hogg, D. W., Lang, D., & Goodman, J. 2013, *PASP*, 125, 306
- Fortney, J. J., Lodders, K., Marley, M. S., & Freedman, R. S. 2008, *ApJ*, 678, 1419
- Fortney, J. J., Marley, M. S., & Barnes, J. W. 2007, *ApJ*, 659, 1661
- Fortney, J. J., Mordasini, C., Nettelmann, N., et al. 2013, *ApJ*, 775, 80
- Fraire, J., Deming, D., Benneke, B., et al. 2014, *Nature*, 513, 526
- Freedman, R. S., Lustig-Yaeger, J., Fortney, J. J., et al. 2014, *ApJS*, 214, 25
- Freikh, R., & Murray-Clay, R. A. 2017, ArXiv e-prints, arXiv:1708.00862
- Gao, P., Marley, M. S., Zahnle, K., Robinson, T. D., & Lewis, N. K. 2017, *AJ*, 153, 139
- Gordon, S., & McBride, B. J. 1994, Computer program for calculation of complex chemical equilibrium compositions and applications, Vol. 1 (National Aeronautics and Space Administration, Office of Management, Scientific and Technical Information Program)
- Griffith, C. A. 2014, *Philosophical Transactions of the Royal Society of London Series A*, 372, 20130086
- Guillot, T. 2010, *A&A*, 520, A27
- Heng, K., & Kitzmann, D. 2017, *MNRAS*, 470, 2972
- Horne, K. 1986, *PASP*, 98, 609
- Kreidberg, L. 2015, *PASP*, 127, 1161
- Kreidberg, L., Bean, J. L., Désert, J.-M., et al. 2014a, *Nature*, 505, 69
- . 2014b, *ApJL*, 793, L27
- Kreidberg, L., Line, M. R., Bean, J. L., et al. 2015, *ApJ*, 814, 66
- Lacis, A. A., & Oinas, V. 1991, *J. Geophys. Res.*, 96, 9027
- Line, M. R., Knutson, H., Wolf, A. S., & Yung, Y. L. 2014, *ApJ*, 783, 70
- Line, M. R., Vasisht, G., Chen, P., Angerhausen, D., & Yung, Y. L. 2011, *ApJ*, 738, 32
- Line, M. R., Wolf, A. S., Zhang, X., et al. 2013, *ApJ*, 775, 137
- Line, M. R., Stevenson, K. B., Bean, J., et al. 2016, *AJ*, 152, 203
- Madhusudhan, N., Amin, M. A., & Kennedy, G. M. 2014, *ApJL*, 794, L12
- Madhusudhan, N., Harrington, J., Stevenson, K. B., et al. 2011, *Nature*, 469, 64

¹ <https://jwst-docs.stsci.edu>

- McCullough, P. R., Crouzet, N., Deming, D., & Madhusudhan, N. 2014, *ApJ*, 791, 55
- Mollière, P., van Boekel, R., Dullemond, C., Henning, T., & Mordasini, C. 2015, *ApJ*, 813, 47
- Mordasini, C., van Boekel, R., Mollière, P., Henning, T., & Benneke, B. 2016, *ApJ*, 832, 41
- Morley, C. V., Fortney, J. J., Marley, M. S., et al. 2012, *ApJ*, 756, 172
- . 2015, *ApJ*, 815, 110
- Morley, C. V., Knutson, H., Line, M., et al. 2017, *AJ*, 153, 86
- Moses, J. I., Madhusudhan, N., Visscher, C., & Freedman, R. S. 2013, *ApJ*, 763, 25
- Močnik, T., Hellier, C., Anderson, D. R., Clark, B. J. M., & Southworth, J. 2017, *MNRAS*, 469, 1622
- Öberg, K. I., Murray-Clay, R., & Bergin, E. A. 2011, *ApJL*, 743, L16
- Pollack, J. B., Hubickyj, O., Bodenheimer, P., et al. 1996, *Icarus*, 124, 62
- Rackham, B. V., Apai, D., & Giampapa, M. S. 2018, *ApJ*, 853, 122
- Saumon, D., Chabrier, G., & van Horn, H. M. 1995, *ApJS*, 99, 713
- Skemer, A. J., Marley, M. S., Hinz, P. M., et al. 2014, *ApJ*, 792, 17
- Stevenson, K. B., Bean, J. L., Seifahrt, A., et al. 2014, *AJ*, 147, 161
- Thorngren, D. P., Fortney, J. J., Murray-Clay, R. A., & Lopez, E. D. 2016, *ApJ*, 831, 64
- Tinetti, G., Tennyson, J., Griffith, C. A., & Waldmann, I. 2012, *Philosophical Transactions of the Royal Society of London Series A*, 370, 2749
- Wakeford, H. R., Visscher, C., Lewis, N. K., et al. 2017, *MNRAS*, 464, 4247
- Zahnle, K., Marley, M. S., Freedman, R. S., Lodders, K., & Fortney, J. J. 2009, *ApJL*, 701, L20
- Zahnle, K. J., & Marley, M. S. 2014, *ApJ*, 797, 41
- Zellem, R. T., Swain, M. R., Roudier, G., et al. 2017, *ApJ*, 844, 27
- Zhou, Y., Apai, D., Lew, B. W. P., & Schneider, G. 2017, *AJ*, 153, 243